

Deformation Mechanisms in Compositionally Complex Polycrystalline CoNi-Base Superalloys: Influence of Temperature, Strain-Rate and Chemistry



A. BEZOLD, L.P. FREUND, A. FÖRNER, J. VÖLKL, L.-K. HUBER, M. GÖKEN,
and S. NEUMEIER

Recent studies revealed the excellent high temperature properties of polycrystalline CoNi-base superalloys. However, their underlying deformation behavior has been reported only scarcely so far. In this work, the deformation mechanisms of four polycrystalline compositionally complex CoNi-base superalloys with slightly varying chemical compositions were investigated by compression and creep experiments at temperatures between 750 °C and 850 °C and strain-rates between 10^{-3} and 10^{-8} s $^{-1}$. In the two (Ta + Ti)-rich alloys, a transition of the deformation mechanism from shearing by APB-coupled dislocation pairs to stacking fault shearing and finally also to microtwinning is observed with decreasing strain-rate and increasing temperature. In contrast, APB-based shearing mechanisms represent the dominant mechanism in both (Al + W)-rich alloys in all conditions. At high temperatures and low strain-rates, dislocation glide-climb processes also contribute to plastic deformation in all alloys. By correlating the underlying defect structures with the mechanical properties of these alloys, it becomes evident that a transition to stacking fault shearing and microtwinning leads to a lower strain-rate dependency and superior high-temperature strength in comparison with APB-based mechanisms. Reasons for the different deformation mechanisms, the influence of segregation processes, the consequences for mechanical properties and implications for a mechanism-based alloy design are discussed.

<https://doi.org/10.1007/s11661-022-06912-x>
© The Author(s) 2022

I. INTRODUCTION

SINCE the discovery of the metastable γ' -Co $_3$ (Al,W) phase in the Co–Al–W system,^[1] research groups around the world investigated the influence of alloying elements on the thermophysical and mechanical properties and the resistance to oxidation in these alloys.^[1–8] Based on these studies, numerous advanced Co-base and CoNi-base superalloys have been developed.^[9–12] While some single-crystalline alloys have already shown

similar high-temperature creep strength as 1st generation Ni-base superalloys,^[10,13–15] it is doubtful, whether this class of material will be able to outperform more advanced single-crystalline Ni-base superalloys due to a missing Re effect^[12,16] and a lower resistance to precipitate shearing at high temperatures.^[17–19] On the other hand, polycrystalline CoNi-base superalloys exhibit a promising property profile consisting of excellent creep strength, good oxidation resistance and a sufficiently large processing window for hot working.^[9,11,20–22]

To understand the deformation behavior of these novel alloys, numerous studies have been conducted on the underlying defect structure of ternary, quaternary and compositionally more complex Co-base and CoNi-base superalloys. These studies revealed that the L1 $_2$ -ordered γ' precipitates, which are coherently embedded in an fcc γ matrix, are sheared by anti-phase boundary (APB)-coupled dislocation pairs or bypassed *via* Orowan looping at lower temperatures.^[2,3,23,24] In contrast to these athermal mechanisms, segregation of alloying elements to dislocations and planar defects plays an important role during high-temperature plastic deformation.^[25–33] Depending on the temperature, the stress and the alloy composition, a large variety of

A. BEZOLD, A. FÖRNER, J. VÖLKL, L.-K. HUBER, M. GÖKEN, and S. NEUMEIER are with the Department of Materials Science & Engineering, Institute I: General Materials Properties, Friedrich-Alexander-Universität Erlangen-Nürnberg, Martensstraße 5, 91058 Erlangen, Germany. Contact e-mail: andreas.bezold@fau.de. L. P. FREUND is with the Department of Materials Science & Engineering, Institute I: General Materials Properties, Friedrich-Alexander-Universität Erlangen-Nürnberg and also with the MTU Aero Engines AG, Dachauer Str. 665, 80995 Munich, Germany.
Manuscript submitted September 14, 2022; accepted November 15, 2022.

Article published online December 3, 2022

different segregation-assisted mechanisms have been observed in this alloy system: shearing under the formation of extended APBs, superlattice intrinsic/extrinsic stacking faults (SISFs/SESFs) or APB-SISF-APB configurations and microtwinning.^[17,19,25,34–36] Even though shearing by APB-coupled dislocation pairs can occur in a completely athermal manner, segregation can also assist this mechanism at higher temperatures.^[37,38]

The segregation of alloying elements to these planar defects leads to a reduction of the planar fault energy and thus the resistance against precipitate shearing, which facilitates the propagation of the shearing dislocations associated with these mechanisms.^[26,29,37] Barba *et al.* developed a model to calculate the propagation velocity of various planar defects and concluded that the propagation velocity increases from APBs to SISFs to SESFs and microtwins in the Ni-base superalloy MD2.^[29,37] Depending on the γ' composition, different elements segregate in different magnitudes to the planar defects.^[25,26,32,36–39] While the transition to segregation-assisted stacking fault shearing is usually associated with softening, it can also lead to strengthening effects. Smith *et al.* and Egan *et al.* observed that the segregation of alloying elements in specific alloy compositions can induce a local phase transformation along the stacking faults and microtwin boundaries, which improves the strength of the alloy by impeding detrimental mechanisms like twin thickening and stacking fault ribbon shearing.^[30,40–42] Furthermore, a transition to stacking fault shearing is associated with a yield strength anomaly in a Co–11Ti–15Cr alloy and extensive work-hardening rates in Ta-containing Co-base and CoNi-base superalloys.^[2,3,24,43]

Despite the wealth of studies on the deformation behavior of Co-base and CoNi-base superalloys at high temperatures, systematic investigations on the influence of varying temperatures and strain-rates are missing. Additionally, only few studies have been conducted on the high temperature deformation behavior of polycrystalline Co- or CoNi-base superalloys.^[35,44] In this work, deformation mechanism maps are created for four slightly different compositionally complex polycrystalline CoNi-base superalloys after constant strain-rate compression and creep experiments at temperatures between 750 °C and 850 °C and strain-rates between 10^{-3} s^{-1} and 10^{-8} s^{-1} . The differences in the underlying defect structures as a function of temperature, strain-rate and composition are evaluated. Additionally, the role of segregation processes during plastic deformation is discussed. Furthermore, the different deformation

mechanisms are correlated with the corresponding mechanical properties to evaluate their influence on the high temperature strength of the investigated alloys.

II. EXPERIMENTAL METHODS

Four polycrystalline CoNi-base superalloys were investigated, whose nominal compositions are given in Table I. CoWAlloy1, PHESA1 and PHESA2 were arc-melted in an Ar atmosphere using raw elements of at least 99.9 pct purity. To improve homogeneity, the samples were turned over and re-melted at least three times. After casting, the specimens were solution heat treated at 1250 °C for 3 h in air and cold-rolled up to a thickness reduction of 40 pct. Subsequently, the specimens were heat treated at 1075 °C for 4 h to obtain a completely recrystallized microstructure. As previously reported,^[11,20] CoWAlloy2 was vacuum arc-melted, cast, homogenized at 1250 °C for 3 h and rolled on a non-heated rolling mill with starting temperatures between 1100 °C and 1150 °C by *Vacuumschmelze GmbH* from a diameter of 40 mm down to 15 mm after casting and homogenization at 1250 °C for 3 h in air. After rolling, a recrystallization heat treatment at 1000 °C for 4h was conducted. An additional two-step aging heat treatment was conducted on all alloys to generate the γ/γ' microstructure, which consisted of 900 °C for 4 h and 750 °C for 16 h with air cooling after each step.

The initial microstructure after processing and heat-treatment was investigated using a *Zeiss Crossbeam 1540 EsB* scanning electron microscope after a sample preparation consisting of grinding with SiC paper up to 4000 grit and polishing with a final step using Struers OPS (fumed silica suspension with a size of 0.25 μm). The median grain size was determined *via* electron backscatter diffraction (EBSD) using an *Oxford Instruments Nordlys2* detector. Additionally, the chemical composition of the γ and γ' phases were determined *via* atom probe tomography using a *CAMECA LEAP 4000X HR*. Atom-probe tips were produced *via* pillar FIB lift-out as described in Reference 45 using a *Zeiss Crossbeam 540 XB*. A pulse fraction of 125 kHz in laser mode with a pulse energy of 50 pJ was used to trigger field evaporation in 1 pct of the pulses. The specimen temperature was set to 49 K.

Compression experiments were conducted to investigate the deformation behavior for a high number of different strain-rate and temperature combinations. Cylindrical compression specimens were obtained by wire spark erosion with a length to diameter ratio of 1.5

Table I. Nominal Composition of CoWAlloy1, CoWAlloy2, PHESA1, PHESA2 in At. Pct

Alloy	Co	Ni	Al	W	Ti	Ta	Cr	Si	Hf	Zr	B	C
CoWAlloy1	bal	32.0	6.0	3.0	2.5	1.5	12.0	0.4	0.1		0.08	
CoWAlloy2	bal	32.0	9.0	5.0	0.3	0.2	12.0	0.4	0.1	0.01	0.08	0.08
PHESA1	bal	35.0	7.5	5.0	1.0	1.0	15.0	0.4	0.1		0.08	
PHESA2	bal	35.0	9.0	5.0	0.3	0.2	15.0	0.4	0.1		0.08	

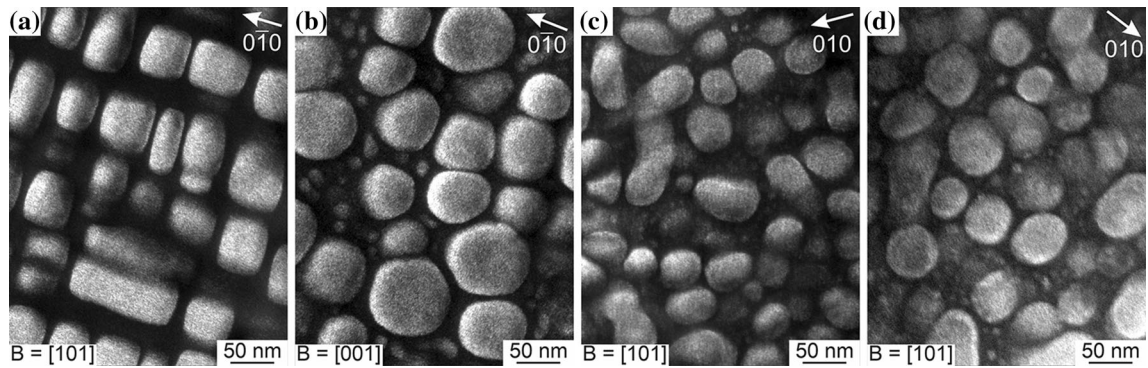


Fig. 1—TEM-DADF images of the γ/γ' microstructure in (a) CoWAlloy1, (b) CoWAlloy2, (c) PHESA1 and (d) PHESA2.

and diameters between 3 and 4 μm depending on sample availability. Subsequently, all surfaces were ground with SiC paper up to 2500 grit. The final height tolerance of the top and bottom faces was less than 10 μm for all specimen. Constant strain-rate compression experiments were conducted using an *Instron 4505* universal testing machine at temperatures between 750 $^{\circ}\text{C}$ and 850 $^{\circ}\text{C}$ and strain-rates of 10^{-3} s^{-1} , 10^{-4} s^{-1} , 10^{-5} s^{-1} and 10^{-6} s^{-1} . Additionally, specimens were crept in a pneumatic creep machine under constant compressive stresses between 300 and 800 MPa in the same temperature range of 750 $^{\circ}\text{C}$ to 850 $^{\circ}\text{C}$. To investigate the underlying defect structures, all experiments were interrupted after reaching 1 to 2 pct plastic strain.

From the inner part of the interrupted specimens and also from the undeformed material, 400 μm thick slices were cut using a precision saw and ground to a thickness of 100 μm with SiC paper up to 4000 grit. The resulting foils were electropolished in an 83.3 pct methanol—16.7 pct nitric acid solution using a *TenuPol-5* at -25°C and 45 V. Subsequently, conventional transmission electron microscopy (TEM) investigations were conducted on a *Philips CM200* at a high voltage of 200 kV. Due to the strong grain orientation dependence of deformation mechanisms,^[46] at least five randomly chosen grains were investigated for each specimen to capture all occurring mechanisms.

III. RESULTS

A. Microstructure

After processing and heat treatment, all alloys exhibit a fully recrystallized grain structure with median grain sizes of 15.8, 24.5 and 18.6 μm for CoWAlloy1, PHESA1 and PHESA2, respectively. As determined previously,^[20] the median grain size of CoWAlloy2 is 8.2 μm , which is lower than the grain size of the other alloys due to the higher plastic deformation prior to recrystallization. Additionally, grain boundary phases precipitated in PHESA1 and PHESA2 with total area fractions of 1.47 and 0.93 pct, see Reference 47.

The γ/γ' microstructure was characterized through TEM using displaced-aperture dark-field (DADF)

imaging as shown in Figure 1. Parameters of the γ/γ' microstructure are summarized in Table II. As determined previously,^[20] primary γ' precipitates form in CoWAlloy1. Due to the different processing conditions for CoWAlloy1 in this study, the primary γ' volume fraction is only 7.5 pct compared to the 18 pct published by Freund.^[48] In CoWAlloy2, PHESA1 and PHESA2, no primary γ' precipitates are observed. The increased (Ni + Cr) to Co content in the PHESA alloys leads to a slightly higher secondary γ' volume fraction and lower secondary γ' size than in the CoWAlloys after the same heat treatment. By changing the (Ta + Ti) to (Al + W) ratio in CoWAlloy1 and PHESA1, no significant differences regarding the γ' volume fraction are determined, although the secondary γ' size decreases. Similarly, the tertiary γ' size is also lower if the (Ta + Ti) to (Al + W) and/or the (Ni + Cr) to Co ratios are higher. The tertiary γ' volume fraction is below 2 pct in CoWAlloy1, PHESA1 and PHESA2, while it is significantly higher in CoWAlloy2 at about 6.7 pct. Nevertheless, the total γ' volume fraction in all four alloys is comparable. The shape of the secondary γ' precipitates in CoWAlloy1 is cuboidal, while the precipitates in the other alloys are spherical indicating a higher lattice misfit in CoWAlloy1 compared to the other alloys.

The composition of both the γ and the γ' phase was determined using APT (see Table III). Results on CoWAlloy1 and CoWAlloy2 have been already published elsewhere.^[48,49] In accordance with literature,^[12,49,50] Co and Cr partition to the γ matrix phase, while Ni, Al, Ti and Ta strongly prefer the γ' precipitate phase. W is slightly enriched in γ' in all alloys. Compared with their respective CoWAlloy counterpart, the alloying elements in the PHESA alloys partition stronger to either the γ or γ' phase. This stronger partitioning behavior is related to the higher Ni content in these alloys.^[50,51]

B. Mechanical Properties

A summary of all conducted mechanical investigations is shown in the form of a Norton plot in Figure 2. Creep experiments are included using the applied true stress and the resulting minimum creep rate. On the other hand, a constant true strain-rate is used during compression testing. Due to the initial work-hardening

Table II. Microstructural Parameters of the Investigated Alloys

Alloy	Prim. γ' VF/pct	Prim. γ' Size/nm	Sec. γ' VF/pct	Sec. γ' Size/nm	Ter. γ' VF/pct	Ter. γ' Size/nm	Grain Size/ μm
CoWAlloy1	7.5 ± 1.4	225.1 ± 54.2	54.0 ± 2.0	52.7 ± 16.2	0.2 ± 0.1	9.7 ± 3.7	15.8
CoWAlloy2	—	—	55.1 ± 1.4	70.0 ± 21.4	6.7 ± 0.4	15.9 ± 4.2	8.2
PHESA1	—	—	60.7 ± 0.5	44.3 ± 11.2	0.6 ± 0.2	6.8 ± 2.6	24.5
PHESA2	—	—	60.0 ± 0.5	54.4 ± 14.1	1.5 ± 0.3	9.2 ± 2.7	18.6

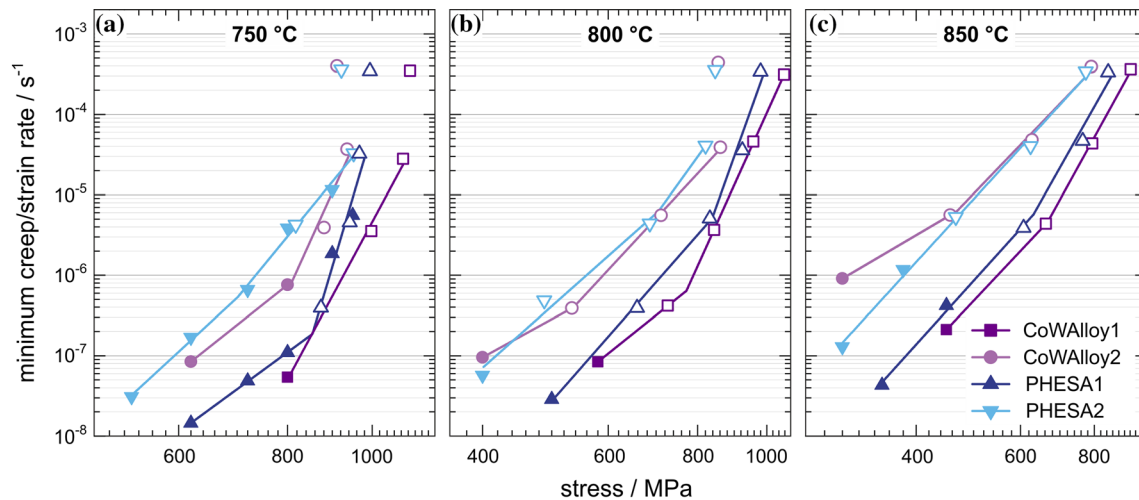


Fig. 2—Norton plot of the investigated alloys at (a) 750 °C, (b) 800 °C and (c) 850 °C. In addition to the creep experiments (filled symbols), the yield strengths at a plastic strain of 1 pct obtained during the constant strain-rate experiments (open symbols) are also included.

and the subsequent increase in the applied stress, the elastic strain increases also during the experiment. In contrast, the elastic strain in the creep experiments is constant after the initial loading. Thus, the effective mean true plastic strain-rate during the compression tests is calculated by dividing the total plastic strain by the total time, in which the alloy is plastically deformed. Furthermore, for experiments, which do not reach the peak stress yet, the stress after 1 pct plastic deformation is used. As shown previously^[47] and in Figure 2(a), this approach shows good agreement between the two types of experiment. Nevertheless, if the alloy still work-hardens after 1 pct, which occurs at low temperatures and high strain-rates, *i.e.*, 750 °C and 10^{-3} s^{-1} (see Figure 2(a)), a deviation from the fitted lines is clearly visible. In the case of CoWAlloy2 and PHESA2, the 1 pct offset stress at this condition is even lower than at a strain-rate of 10^{-4} s^{-1} due to the higher work-hardening rates in the latter case. The stress–strain and creep curves of all experiments are shown in the supplementary Figure S1 and S2 (refer to electronic supplementary material), respectively.

Figure 2 reveals the significance of the Ta and Ti additions in PHESA1 and CoWAlloy1 as the strength is significantly enhanced in comparison to PHESA2 and CoWAlloy2 at all investigated temperatures. In contrast, the respective alloys of the CoWAlloy series perform only slightly better compared to their PHESA counterparts at 750 °C, while the difference diminishes

with increasing temperature. Hence, the impact of the Co to Ni + Cr ratio is apparently significantly lower than that of the Al(+ W) to (Ta + Ti) ratio in these alloys. To rationalize the differences in performance between the four alloys, the underlying defect structures of all tests shown in Figure 2 are investigated using CTEM.

C. Deformation Mechanisms

Overviews of the deformation mechanisms occurring in CoWAlloy1, CoWAlloy2, PHESA1 and PHESA2 are shown in Figures 3, 4, 5 and 6, respectively.

At a low temperature of 750 °C and a strain-rate of 10^{-3} s^{-1} , the defect structure of CoWAlloy1 is mainly composed of stacking faults in the γ matrix channels, which extend from one γ/γ' interface to another one as shown in Figure 3(a). APB-coupled dislocation pairs shearing the γ' precipitates are also observed. Occasionally stacking faults are able to extend across the γ/γ' microstructure. At a higher temperature of 800 °C, the number of APB-coupled dislocation pairs decreases, while the contribution of stacking fault shearing increases (see Figure 3(b)). This transition in the γ' shearing mechanism continues when the temperature is further increased and/or the strain-rate is reduced (see Figures 3(c) through (e)). Additionally, more elongated stacking faults are observed. At even lower strain-rates, microtwinning is also observed (Figure 3(d)). Besides

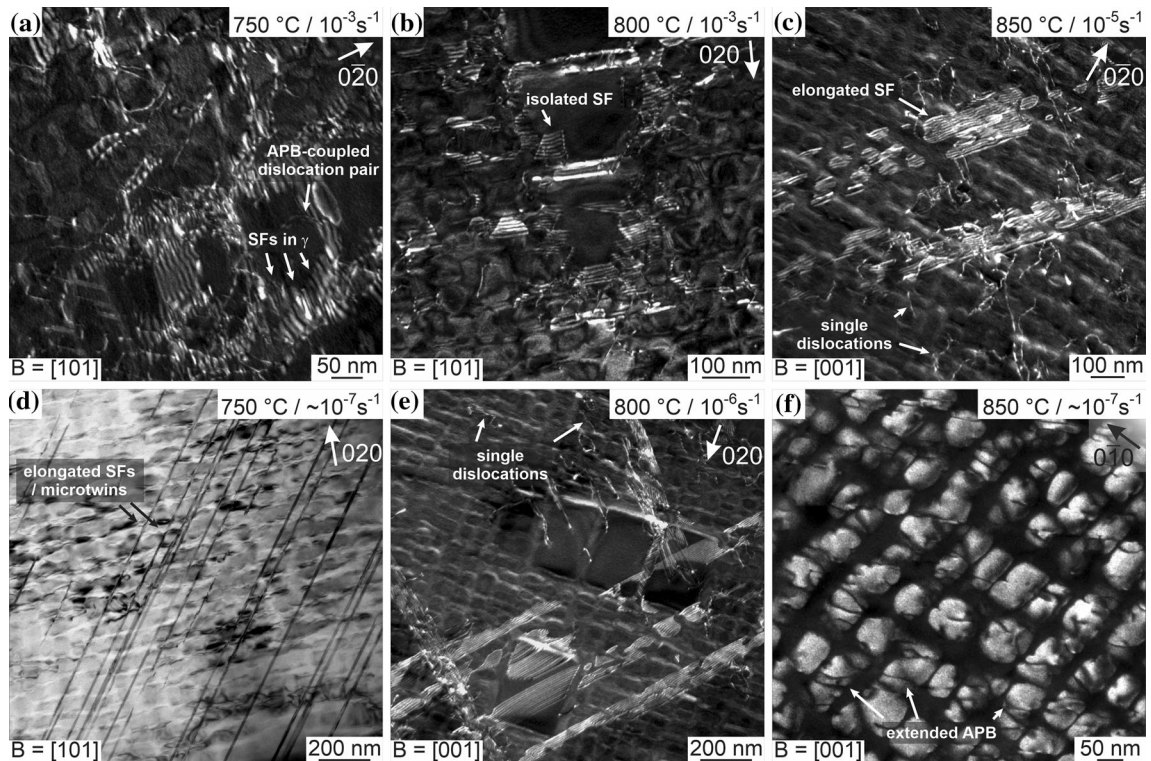


Fig. 3—TEM investigations on CoWAlloy1 after selected (a, b, c, e) constant strain-rate and (d, f) creep experiments interrupted at a plastic strain of about 1 pct. (a) 750 °C and 10^{-3} s^{-1} , WBDF image with $\mathbf{g} = 0\text{--}20$ ($\mathbf{g}\text{--}3 \mathbf{g}$), (b) 800 °C and 10^{-3} s^{-1} , WBDF image with $\mathbf{g} = 020$ ($\mathbf{g}\text{--}3 \mathbf{g}$), (c) 850 °C and 10^{-5} s^{-1} , WBDF image with $\mathbf{g} = 0\text{--}20$ ($\mathbf{g}\text{--}3 \mathbf{g}$), (d) 750 °C and 800 MPa, BF image with $\mathbf{g} = 020$, (e) 800 °C and 10^{-6} s^{-1} , WBDF image with $\mathbf{g} = 020$ ($\mathbf{g}\text{--}3 \mathbf{g}$) and (f) 850 °C and 450 MPa, DADF image with $\mathbf{g} = 0\text{--}10$.

stacking faults and microtwinning, also an increased density of single dislocations, which bypass the precipitates through glide-climb motion, is observed at higher temperatures and lower strain-rates (see Figures 3(c) and (e)). Furthermore, single superpartial dislocations are able to shear the precipitates while leaving extended APBs in their wake at 850 °C and a strain-rate of about 10^{-7} s^{-1} as shown in Figure 3(f). Nevertheless, stacking fault shearing and microtwinning also occur at these creep conditions.

At low temperatures and high strain-rates (750 °C and 10^{-3} s^{-1}), the γ' precipitates in CoWAlloy2 are sheared by APB-coupled dislocation pairs similar to CoWAlloy1 (Figure 4(a)). Extended stacking faults have not been observed across the γ/γ' microstructure, even though dislocations also dissociate in the γ matrix channels under stacking fault formation. Comparable defect structures are also observed at higher temperatures and similar strain-rates as shown in Figures 4(b) and (c). At lower strain-rates, stacking fault shearing starts to occur and its contribution increases with decreasing strain-rate. Nevertheless, shearing by APB-coupled dislocations pairs still remains a significant deformation mechanism at lower strain-rates as shown in Figure 4(d). Extended stacking faults, stacking fault ribbons and microtwins are also occasionally observed at these low strain-rates, although their density is relatively low compared to the density of APB-coupled dislocation pairs or isolated stacking faults. At

higher temperatures and lower strain-rates, single superpartial dislocations are able to shear the γ' precipitates under the formation of extended APBs as shown in Figures 4(e) and (f). While these defect structures coexist with stacking faults and APB-coupled dislocations at 800 °C and 10^{-5} s^{-1} , their occurrence increases with increasing temperature and decreasing strain-rate. In addition, single dislocations are also able to overcome the precipitates *via* glide-climb motion at higher temperatures and lower strain-rates.

Similar to the other two alloys mentioned above, APB-coupled dislocation pairs shear through the γ/γ' microstructure in PHESA1 at low temperatures and high strain-rates. However, as shown in Figure 5(a), the resulting defect structure looks different. No single dislocations, which extend from one γ/γ' interface to another or which are deposited as interfacial dislocations, are observed but only APB-coupled dislocation pairs. In contrast to both CoWAlloys, a fourfold dissociation of the coupled superpartial dislocation pairs can be observed using WBDF as shown in supplementary Figure S3. As such a dissociation could not be resolved in both CoWAlloys, this observation indicates an even lower stacking fault energy of the γ matrix in PHESA1 compared to the CoWAlloys. At the highest investigated strain-rate of 10^{-3} s^{-1} , plastic deformation is solely carried out by APB-coupled dislocation pairs at all temperatures (see for example Figure 5(b) for 800 °C). With decreasing strain-rate, the

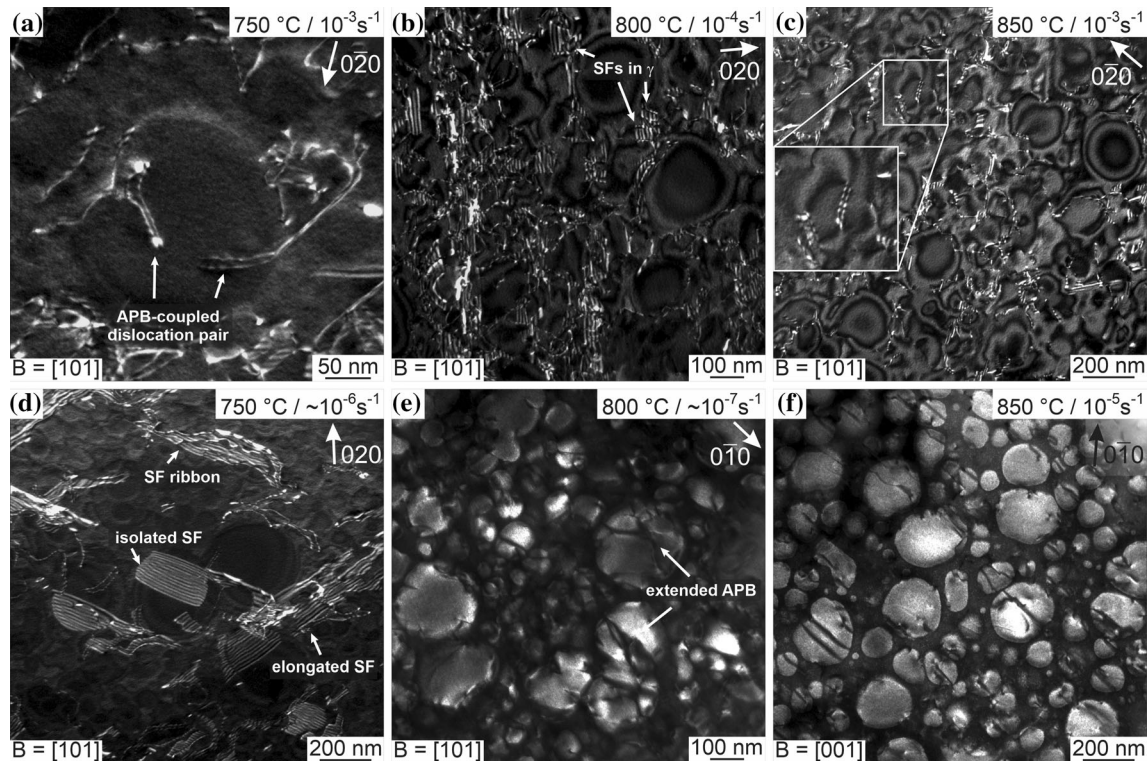


Fig. 4—TEM investigations on CoWAlloy2 after selected (*a, b, c, f*) constant strain-rate and (*d, e*) creep experiments interrupted at a plastic strain of about 1 pct. (a) 750 °C and 10^{-3} s^{-1} , WBDF image with $g = 0\text{-}20$ ($g\text{-}3 \text{ g}$), (b) 800 °C and 10^{-4} s^{-1} , WBDF image with $g = 020$ ($g\text{-}3 \text{ g}$), (c) 850 °C and 10^{-3} s^{-1} , WBDF image with $g = 0\text{-}20$ ($g\text{-}3 \text{ g}$), (d) 750 °C and 800 MPa, WBDF image with $g = 020$ ($g\text{-}3 \text{ g}$), (e) 800 °C and 400 MPa, DADF image with $g = 0\text{-}10$ and (f) 850 °C and 10^{-5} s^{-1} , DADF image with $g = 0\text{-}10$.

acting deformation mechanisms in PHESA1 transitions to stacking fault shearing (Figure 5(c) through (f)) and subsequently also microtwinning similar to CoWAlloy1 (Figures 5(d) and (f)). As shown in Figure 5(e), single dislocations also contribute to plastic deformation *via* glide and climb motion at 800 °C and 10^{-6} s^{-1} , which is also observed if the temperature is further increased and/or the strain-rate is lowered. Extended APBs created by single superpartial dislocations were not observed in any of the investigated conditions in PHESA1.

As shown in Figure 6, shearing by APB-coupled dislocation pairs occurs at all investigated conditions in PHESA2. Similar to PHESA1, the superpartial dislocations dissociate in the γ matrix under the formation of stacking faults (see Figures 6(a) and (b)). Additionally, two other mechanisms are observed in PHESA2. At low temperatures and low strain-rates, stacking fault shearing, in the form of stacking fault ribbons or isolated stacking faults, is also observed occasionally (see Figures 6(d) and (e)). Despite the similarities to CoWAlloy2, no extended APBs have been found in any of the specimens. However, single dislocations are also observed in PHESA2 at high temperatures and low strain-rates as shown in Figures 6(e) and (f). Nevertheless, except for high temperatures and low strain-rates (850 °C and $< 10^{-6} \text{ s}^{-1}$), shearing by APB-coupled dislocation pairs is the dominant deformation mechanism at all conditions.

IV. DISCUSSION

Previous investigations on the defect structures in Co-base and CoNi-base superalloys revealed the occurrence of a large variety of different deformation mechanisms. While most of these studies focused on single-crystalline alloys with orientations close to the [001] zone axis, numerous parameters, *i.e.*, the applied stress, the temperature, the alloy composition and the microstructure, still varied significantly, which prevents a thorough evaluation of the temperature and strain-rate dependence of various mechanisms and their impact on creep strength. The systematic investigations on the defect structures in CoWAlloy1, CoWAlloy2, PHESA1 and PHESA2 at temperatures between 750 °C and 850 °C and strain-rates between 10^{-3} s^{-1} and about 10^{-8} s^{-1} provide an opportunity to construct deformation mechanism maps and to correlate the transitions in the deformation behavior with the mechanical properties.

As shown in Figure 7, the small chemical differences in the four investigated alloys lead to drastic changes in the underlying deformation behavior. The (Ta + Ti)-rich alloys, CoWAlloy1 and PHESA1, show qualitatively a similar deformation behavior that transitions from γ' shearing by APB-coupled dislocation pairs to stacking fault shearing, microtwinning and dislocation glide-climb with increasing temperature and decreasing strain-rate. However, extended APBs created by single superpartial

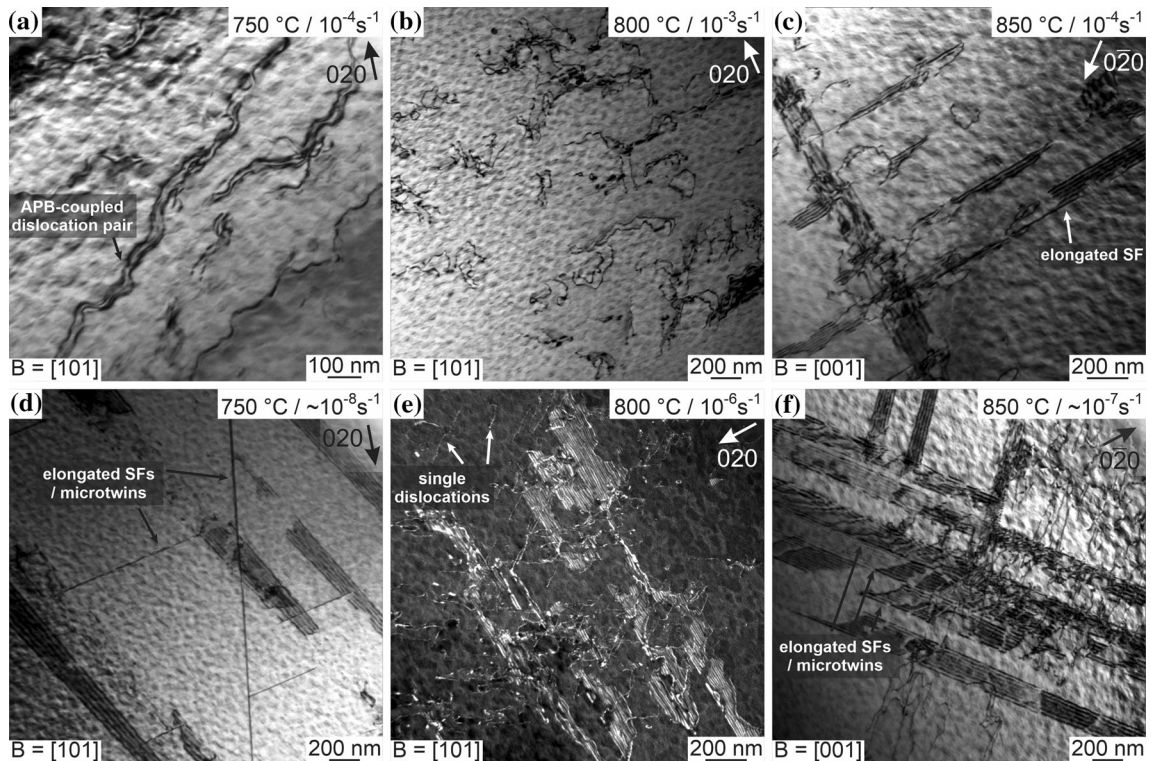


Fig. 5—TEM investigations on PHESA1 after selected (a, b, c, e) constant strain-rate and (d, f) creep experiments interrupted at a plastic strain of about 1 pct. (a) 750 °C and 10^{-4} s^{-1} , BF image with $\mathbf{g} = 020$, (b) 800 °C and 10^{-3} s^{-1} , BF image with $\mathbf{g} = 020$, (c) 850 °C and 10^{-4} s^{-1} , BF image with $\mathbf{g} = 0-20$, (d) 750 °C and 620 MPa, BF image with $\mathbf{g} = 020$, (e) 800 °C and 10^{-6} s^{-1} , WBDF image with $\mathbf{g} = 020$ ($\mathbf{g}-3 \mathbf{g}$) and (f) 850 °C and 380 MPa, BF image with $\mathbf{g} = 0-20$.

dislocations are only observed in CoWAlloy1. Additionally, the different regimes are shifted relative to each other, whereby especially shearing by APB-coupled dislocation pairs remains dominant over a larger temperature/strain-rate field in PHESA1. Additionally, the occurrence of the segregation- or diffusion-assisted mechanisms is shifted to an order of magnitude lower strain-rates at comparable temperatures in PHESA1.

In contrast to CoWAlloy1 and PHESA1, their (Al + W)-rich counterparts show a different deformation behavior. While a transition from shearing by APB-coupled dislocation pairs to stacking fault shearing also occurs in CoWAlloy2, microtwinning is not observed at the investigated strain-rates. In a previous study, Freund *et al.* found microtwinning in CoWAlloy2 after tensile creep at 750 °C and 530 MPa, which indicates that the transition to microtwinning still occurs in CoWAlloy2 if the strain-rate is low enough.^[35] With increasing temperature, single superpartial dislocations are able to shear through the γ/γ' microstructure and represent the dominant shearing mechanism. This mechanism is not observed in PHESA2, which deforms predominantly by APB-coupled dislocation pairs at all investigated conditions except for high temperatures and low strain-rates, at which glide-climb motion by single superpartials becomes the dominant occurring mechanism.

Besides temperature and stress, various other factors are also considered to influence the acting deformation mechanism: grain orientation, tertiary γ' volume

fraction, planar fault energies and segregation processes.^[24-27,37,46,52,53] As shown by the extensive work of León-Cázarez *et al.*,^[46] the grain orientation significantly influences the type of stacking fault shearing. Thus, stacking fault shearing is summarized in one category in Figure 7 and the focus is laid on the transition of athermal mechanisms to specific segregation-assisted mechanisms. Due to the strong grain orientation dependence, various grains have been observed in each specimen and the dominantly occurring mechanisms have been summarized in Figure 7. Previous work by Viswanathan *et al.* showed that a substantial tertiary γ' volume fraction can also facilitate a transition to stacking fault shearing.^[52] However, in this work, the alloys with low tertiary γ' volume fraction deform extensively by stacking faults and microtwins in contrast to the alloys with a higher tertiary γ' volume fraction, which deform by APB-coupled dislocation pairs. Since the total tertiary γ' volume fraction is less than 2 pct for both PHESA alloys and CoWAlloy1 and the operating deformation mechanisms differ strongly, the tertiary γ' volume fraction does not appear to play a significant role in the investigated alloys at the selected test conditions. Hence, the transition to the segregation-assisted mechanisms and the differences between the alloys is related to different planar fault energies and/or segregation processes.

Based on the work of Crudden *et al.*,^[54] the unsegregated APB energies E_{APB} of the different γ' phases are calculated as follows:

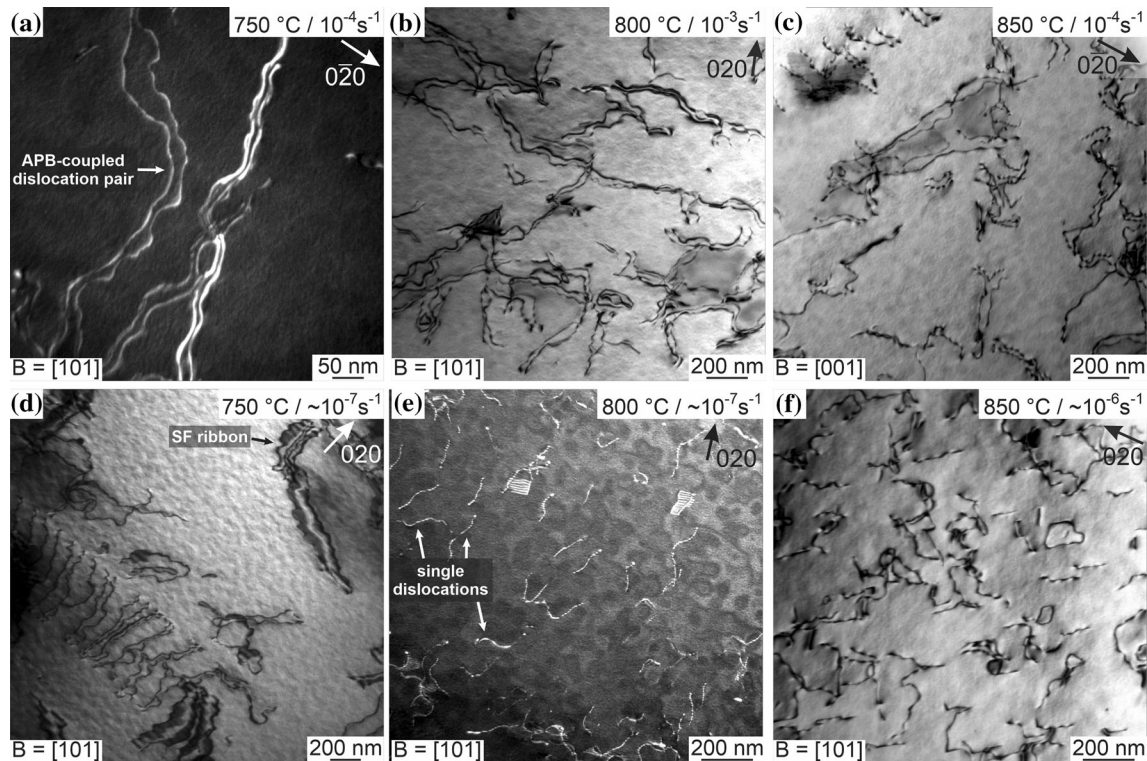


Fig. 6—TEM investigations on PHESA2 after selected (a-c) constant strain-rate and (d-f) creep experiments interrupted at a plastic strain of about 1 pct. (a) 750 °C and 10^{-4} s^{-1} , WBDF image with $\mathbf{g} = 0\text{-}20$ (g-3 g), (b) 800 °C and 10^{-3} s^{-1} , BF image with $\mathbf{g} = 020$, (c) 850 °C and 10^{-4} s^{-1} , BF image with $\mathbf{g} = 0\text{-}20$, (d) 750 °C and 620 MPa, BF image with $\mathbf{g} = 020$, (e) 800 °C and 400 MPa, WBDF image with 020 (g-3 g) and (f) 850 °C and 350 MPa, BF image with $\mathbf{g} = 020$.

$$E_{APB} = E_{APB}^0 + \sum_{i=1}^n (k_i x_i)$$

where E_{APB}^0 is the APB energy for Ni_3Al measured by Kruml *et al.* [55], x_i is the solute concentration of element i in the γ' precipitates and k_i are element-specific coefficients for the change in APB energy per at. pct.

Since the γ' precipitates in the investigated CoNi-base superalloys consist mainly of Ni, the element specific coefficients k_i from References 54 and 56 are used, which have been derived *via* density functional theory (DFT) calculations. By inserting the γ' composition as determined by atom-probe tomography (see Table III), the APB energies of CoWAlloy1, CoWAlloy2, PHESA1 and PHESA2 are determined to be equal to 335, 162, 235 and 162 mJ/m^2 . Hence, the addition of only moderate amounts of Ta and Ti already leads to drastic increases in the APB energy.

Besides increasing the APB energy, Ta and Ti are known to increase the SISF and CSF energy of $\text{Ni}_3(\text{Al},\text{X})$. [57,58] Initial investigations of the influence of Ta and Ti in $\text{Co}_3(\text{A},\text{W})$ also reported an increase of the SISF energy in this system. [54,59] However, recent DFT calculations revealed that Ta is actually predicted to decrease the SISF energy if the supercell is fully

relaxed. [33] Studies on the influence of Ta and Ti in the $(\text{Co},\text{Ni})_3(\text{Al},\text{X})$ system are currently missing and are needed to clarify the precise role of Ta and Ti on the stacking fault energy in CoNi-base superalloys and on the acting deformation mechanism.

Nevertheless, phase-field simulations by Feng *et al.* revealed that single superpartials can only shear the γ' precipitates by leaving an APB in their wake if the APB energy is low enough. [60] While segregation of alloying elements certainly leads to a reduction of the APB energy, the higher initial barrier in the (Ta + Ti)-rich alloys might be the reason why these alloys do not predominantly deform by APB-based mechanisms at lower strain-rates in contrast to the (Al + W)-rich alloys.

Even though the mechanical properties of the alloys cannot be compared on an absolute scale due to differences in the γ/γ' structure and grain size, the strain-rate dependence, *i.e.*, the decrease in strength with decreasing strain-rate, can be correlated with the different defect structures. In Figure 8, the 1 pct offset stress $R_{p,1}$ at a true strain-rate of 10^{-4} s^{-1} is plotted with the stress to obtain a creep rate of 10^{-7} s^{-1} . The corresponding deformation mechanisms are also shown. As evidenced in Figure 8(a), a transition to stacking fault shearing and microtwinning is associated with a lower

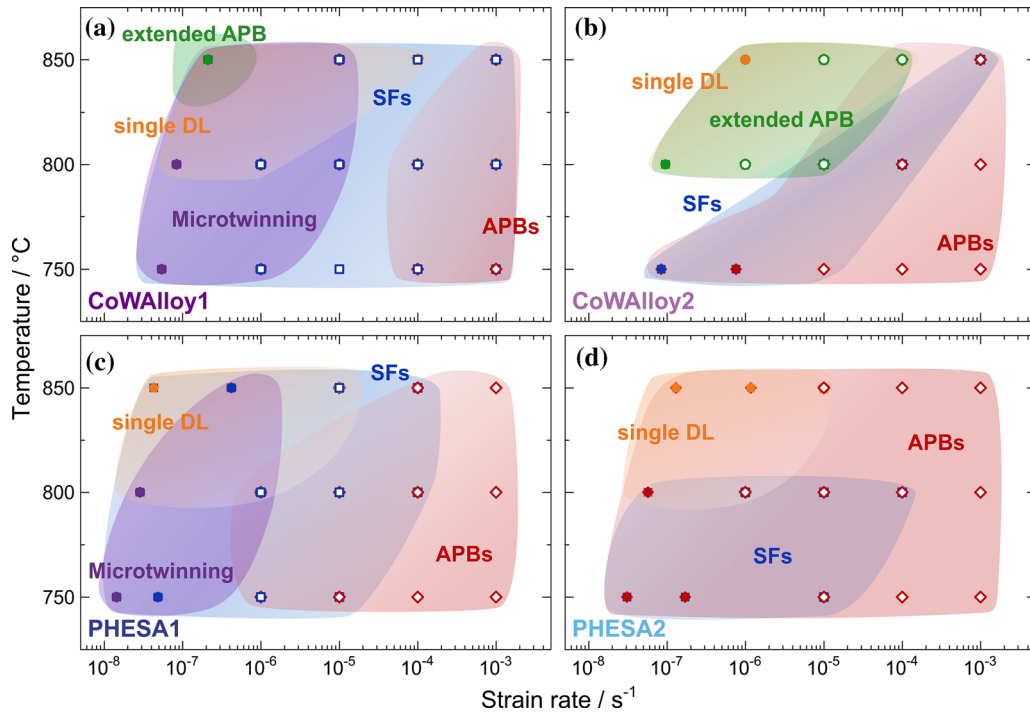


Fig. 7—Deformation mechanism maps of (a) CoWAlloy1, (b) CoWAlloy2, (c) PHESA1 and (d) PHESA2 as a function of strain rate and temperature. Full and open symbols refer to constant strain-rate and creep experiments, respectively.

Table III. Chemical Composition of the γ and γ' Phase in the Investigated Alloys as Determined by APT

Alloy	Phase	Co	Ni	Al	W	Ti	Ta	Cr
CoWAlloy1	γ'	27.55	43.50	11.98	3.66	5.65	3.59	3.19
	γ	50.93	20.24	2.83	3.37	0.72	0.26	20.61
CoWAlloy2	γ'	32.80	39.37	14.53	6.06	0.50	0.37	5.45
	γ	49.00	21.26	3.63	4.36	0.04	0.03	20.95
PHESA1	γ'	24.52	50.54	13.41	4.12	2.34	1.47	3.08
	γ	45.66	21.53	2.26	3.11	0.13	0.05	27.03
PHESA2	γ'	25.67	49.29	15.95	2.98	0.74	0.23	4.61
	γ	43.92	21.91	2.96	2.66	0.06	0.02	27.79

drop in strength in the (Ta + Ti)-rich alloys compared to their (Al + W)-rich counterparts at 750 °C. With increasing temperature and the occurrence of glide and climb motion of single superpartial dislocations, the strain rate dependence increases in all alloys, whereby it is still slightly lower in the (Ta + Ti)-rich alloys at 800 °C (Figure 8(b)). However, at 850 °C, the stress difference is slightly lower in PHESA2, while the one in CoWAlloy2 increases (Figure 8(c)), which might be related to the lower grain size of CoWAlloy2 in comparison to the other three alloys (see Table II). Since the propagation of stacking faults and microtwins are strongly segregation-assisted,^[29,37] higher temperatures lead to higher dislocation velocities. This might explain the increasing strain-rate dependence in the (Ta + Ti)-rich alloys compared to the (Al + W)-rich alloys with increasing temperature. Nevertheless, the beneficial effect of stacking fault shearing and

microtwinning on the high temperature strength of these alloys at 750 °C is evident.

Based on the investigations in this study, a general guideline for a mechanism-based alloy design for high strength polycrystalline CoNi-base superalloys can be derived. As shown above, a transition to stacking fault shearing and microtwinning significantly reduces the strain-rate dependence of the alloy and improves the high temperature strength at 750 °C. Besides these mechanisms, no other mechanism contributes to plastic deformation at these conditions in CoWAlloy1 and PHESA1. While the exact reason for this behavior is not known as of now, the strong increase in APB energy in these alloys compared to CoWAlloy2 and PHESA2 might play an important role. As deformation is solely carried by stacking fault shearing and microtwinning, the strength can be further improved by preventing microtwinning and stacking fault ribbons by phase

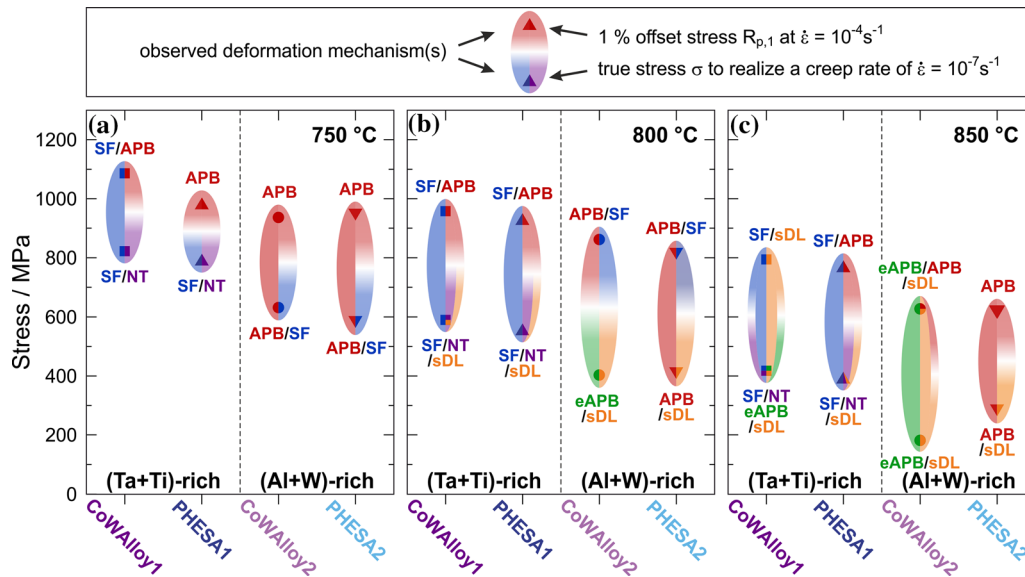


Fig. 8—Correlation of the strain-rate dependence of CoWAlloy1, CoWAlloy2, PHESA1 and PHESA2 and the occurring deformation mechanisms at (a) 750 °C, (b) 800 °C and (c) 850 °C using the 1 pct offset stress $R_{p,1}$ at a strain rate of 10^{-4} s^{-1} and the stress to obtain a creep rate of 10^{-7} s^{-1} . The deformation mechanisms are indicated using the same color code as in Fig. 7 (Color figure online).

transformation strengthening and reducing the propagation velocity of the remaining extended stacking faults. Thus, a mechanism-based alloy design strategy should consider both the segregation of the alloying elements and the unsegregated planar fault energies to tailor the acting deformation mechanism while simultaneously optimizing the segregation behavior.

V. SUMMARY AND CONCLUSION

This study investigated the influence of temperature and strain-rate on the resulting deformation mechanism in four compositionally complex CoNi-base superalloys with slightly different compositions. The following conclusions can be drawn:

- Additions of Ta and Ti significantly improve the high temperature strength of polycrystalline CoNi-base superalloys over a large temperature and strain-rate regime.
- With increasing temperature and decreasing strain-rate, the active deformation mechanism transitions from shearing by APB-coupled dislocation pairs to a segregation-assisted shearing mechanism and finally glide-climb of single superpartial dislocations in all alloys.
- The type of segregation-assisted shearing mechanism strongly depends on the alloy composition. In the Ta- and Ti-containing alloys, extensive stacking fault shearing and microtwinning is observed, while the Al- and W-rich alloys predominantly deform by APB-based mechanism.
- A transition to stacking fault shearing and microtwinning is associated with a lower strain-rate dependence and superior high temperature strength

in comparison to shearing by APB-coupled dislocation pairs.

ACKNOWLEDGMENTS

The authors acknowledge funding from the German Research Foundation (Deutsche Forschungsgemeinschaft DFG) through project NE 1733/2-1 within the priority program SPP 2006 “Compositionally Complex Alloys - High Entropy Alloys”.

CONFLICT OF INTEREST

The authors declare that they have no known competing financial interests or personal relationships that could have appeared to influence the work reported in this paper.

FUNDING

Open Access funding enabled and organized by Projekt DEAL.

OPEN ACCESS

This article is licensed under a Creative Commons Attribution 4.0 International License, which permits use, sharing, adaptation, distribution and reproduction in any medium or format, as long as you give appro-

appropriate credit to the original author(s) and the source, provide a link to the Creative Commons licence, and indicate if changes were made. The images or other third party material in this article are included in the article's Creative Commons licence, unless indicated otherwise in a credit line to the material. If material is not included in the article's Creative Commons licence and your intended use is not permitted by statutory regulation or exceeds the permitted use, you will need to obtain permission directly from the copyright holder. To view a copy of this licence, visit <http://creativecommons.org/licenses/by/4.0/>.

SUPPLEMENTARY INFORMATION

The online version contains supplementary material available at <https://doi.org/10.1007/s11661-022-06912-x>.

REFERENCES

1. J. Sato, T. Omori, K. Oikawa, I. Ohnuma, R. Kainuma, and K. Ishida: *Science*, 2006, vol. 312, pp. 90–91.
2. A. Suzuki, G.C. DeNolf, and T.M. Pollock: *Scr. Mater.*, 2007, vol. 56, pp. 385–88.
3. A. Suzuki and T.M. Pollock: *Acta Mater.*, 2008, vol. 56, pp. 1288–97.
4. A. Bauer, S. Neumeier, F. Pyczak, and M. Göken: *Scr. Mater.*, 2010, vol. 63, pp. 1197–1200.
5. S. Meher, H.-Y. Yan, S. Nag, D. Dye, and R. Banerjee: *Scr. Mater.*, 2012, vol. 67, pp. 850–53.
6. F. Xue, M. Wang, and Q. Feng: in *Superalloys 2012*, TMS, Warrendale, 2012, pp. 813–21.
7. L. Klein, Y. Shen, M.S. Killian, and S. Virtanen: *Corros. Sci.*, 2011, vol. 53, pp. 2713–20.
8. L. Klein, M.S. Killian, and S. Virtanen: *Corros. Sci.*, 2013, vol. 69, pp. 43–49.
9. M. Knop, P. Mulvey, F. Ismail, A. Radecka, K.M. Rahman, T.C. Lindley, B.A. Shollock, M.C. Hardy, M.P. Moody, T.L. Martin, P.A.J. Bagot, and D. Dye: *JOM*, 2014, vol. 66, pp. 2495–2501.
10. M.S. Titus, A. Suzuki, and T.M. Pollock: *Scr. Mater.*, 2012, vol. 66, pp. 574–77.
11. S. Neumeier, L.P. Freund, and M. Göken: *Scr. Mater.*, 2015, vol. 109, pp. 104–07.
12. N. Volz, C.H. Zenk, R. Cherukuri, T. Kalfhaus, M. Weiser, S.K. Mäkinen, C. Betzing, M. Lenz, B. Gault, S.G. Fries, J. Schreuer, R. Vaßen, S. Virtanen, D. Raabe, E. Spiecker, S. Neumeier, and M. Göken: *Metall. Mater. Trans. A.*, 2018, vol. 49A, pp. 4099–109.
13. M.S. Titus, A. Suzuki, and T.M. Pollock: in *Superalloys 2012*, TMS, Warrendale, 2012, pp. 823–32.
14. M.S. Titus, L.H. Rettberg, and T.M. Pollock: in *Superalloys 2016*, M. Hardy, E. Huron, U. Glatzel, B. Griffin, B. Lewis, C. Rae, V. Seetharaman, and S. Tin, eds., John Wiley & Sons, Inc., Hoboken, NJ, 2016, pp. 141–8.
15. A. Bezold, N. Volz, F. Xue, C.H. Zenk, S. Neumeier, and M. Göken: *Metall. Mater. Trans. A*, 2020, vol. 51A, pp. 1567–74.
16. M. Kolb, C.H. Zenk, A. Kirzinger, I. Povstugar, D. Raabe, S. Neumeier, and M. Göken: *J. Mater. Res.*, 2017, vol. 32, pp. 2551–59.
17. M.S. Titus, Y.M. Eggeler, A. Suzuki, and T.M. Pollock: *Acta Mater.*, 2015, vol. 82, pp. 530–39.
18. F. Xue, C.H. Zenk, L.P. Freund, M. Hoelzel, S. Neumeier, and M. Göken: *Scr. Mater.*, 2018, vol. 142, pp. 129–32.
19. M. Lenz, Y.M. Eggeler, J. Müller, C.H. Zenk, N. Volz, P. Wollgramm, G. Eggeler, S. Neumeier, M. Göken, and E. Spiecker: *Acta Mater.*, 2019, vol. 166, pp. 597–610.
20. L.P. Freund, S. Giese, D. Schwimmer, H.W. Höppel, S. Neumeier, and M. Göken: *J. Mater. Res.*, 2017, vol. 32, pp. 4475–82.
21. Y. Zhang, H. Fu, X. Zhou, Y. Zhang, and J. Xie: *Intermetallics*, 2019, vol. 112, p. 106543.
22. X. Zhuang, S. Lu, L. Li, and Q. Feng: *Mater. Sci. Eng. A*, 2020, vol. 780, p. 139219.
23. Z. Fan, C. Wang, C. Zhang, Y. Yu, H. Chen, and Z. Yang: *Mater. Sci. Eng. A*, 2018, vol. 735, pp. 114–20.
24. A. Bezold, N. Volz, M. Lenz, N. Karpstein, C.H. Zenk, E. Spiecker, M. Göken, and S. Neumeier: *Acta Mater.*, 2022, vol. 227, p. 117702.
25. Y.M. Eggeler, J. Müller, M.S. Titus, A. Suzuki, T.M. Pollock, and E. Spiecker: *Acta Mater.*, 2016, vol. 113, pp. 335–49.
26. M.S. Titus, A. Mottura, G. Babu Viswanathan, A. Suzuki, M.J. Mills, and T.M. Pollock: *Acta Mater.*, 2015, vol. 89, pp. 423–37.
27. T.M. Smith, R.R. Unocic, H. Deutchman, and M.J. Mills: *Mater. High Temp.*, 2016, vol. 33, pp. 372–83.
28. D. Barba, S. Pedrazzini, A. Vilalta-Clemente, A.J. Wilkinson, M.P. Moody, P.A.J. Bagot, A. Jérusalem, and R.C. Reed: *Scr. Mater.*, 2017, vol. 127, pp. 37–40.
29. D. Barba, E. Alabort, S. Pedrazzini, D.M. Collins, A.J. Wilkinson, P.A.J. Bagot, M.P. Moody, C. Atkinson, A. Jérusalem, and R.C. Reed: *Acta Mater.*, 2017, vol. 135, pp. 314–29.
30. T.M. Smith, B.D. Esser, N. Antolin, G.B. Viswanathan, T. Hanlon, A. Wessman, D. Mourer, W. Windl, D.W. McComb, and M.J. Mills: *Acta Mater.*, 2015, vol. 100, pp. 19–31.
31. T.M. Smith, Y. Rao, Y. Wang, M. Ghazisaeidi, and M.J. Mills: *Acta Mater.*, 2017, vol. 141, pp. 261–72.
32. S.K. Mäkinen, A. Kumar, M. Lenz, P. Kontis, T. Meiners, C. Zenk, S. Zaefferer, G. Eggeler, S. Neumeier, E. Spiecker, D. Raabe, and B. Gault: *Acta Mater.*, 2018, vol. 155, pp. 362–71.
33. N. Volz, F. Xue, C.H. Zenk, A. Bezold, S. Gabel, A.P.A. Subramanyam, R. Drautz, T. Hammerschmidt, S.K. Mäkinen, B. Gault, M. Göken, and S. Neumeier: *Acta Mater.*, 2021, vol. 214, p. 117019.
34. Y.M. Eggeler, M.S. Titus, A. Suzuki, and T.M. Pollock: *Acta Mater.*, 2014, vol. 77, pp. 352–59.
35. L.P. Freund, O.M.D.M. Messé, J.S. Barnard, M. Göken, S. Neumeier, and C.M.F. Rae: *Acta Mater.*, 2017, vol. 123, pp. 295–304.
36. M. Lenz, M. Wu, and E. Spiecker: *Acta Mater.*, 2020, vol. 191, pp. 270–79.
37. D. Barba, T.M. Smith, J. Miao, M.J. Mills, and R.C. Reed: *Metall. Mater. Trans. A.*, 2018, vol. 49A, pp. 4173–185.
38. S.K. Mäkinen, M. Lenz, S. Neumeier, E. Spiecker, D. Raabe, and B. Gault: *Scr. Mater.*, 2018, vol. 157, pp. 62–66.
39. M. Lenz, M. Wu, J. He, S.K. Mäkinen, B. Gault, D. Raabe, S. Neumeier, and E. Spiecker: in *Superalloys 2020*, S. Tin, M. Hardy, J. Clews, J. Cormier, Q. Feng, J. Marcin, C. O'Brien, and A. Suzuki, eds., Springer, Cham, 2020, pp. 920–28.
40. T.M. Smith, B.D. Esser, N. Antolin, A. Carlsson, R.E.A. Williams, A. Wessman, T. Hanlon, H.L. Fraser, W. Windl, D.W. McComb, and M.J. Mills: *Nat. Commun.*, 2016, vol. 7, p. 13434.
41. T.M. Smith, B.S. Good, T.P. Gabb, B.D. Esser, A.J. Egan, L.J. Evans, D.W. McComb, and M.J. Mills: *Acta Mater.*, 2019, vol. 172, pp. 55–65.
42. A.J. Egan, Y. Rao, G.B. Viswanathan, T.M. Smith, M. Ghazisaeidi, S. Tin, and M.J. Mills: in *Superalloys 2020*, S. Tin, M. Hardy, J. Clews, J. Cormier, Q. Feng, J. Marcin, C. O'Brien, and A. Suzuki, eds., Springer, Cham, 2020, pp. 640–50.
43. A. Bezold, N. Volz, M. Lenz, C.H. Zenk, E. Spiecker, M. Mills, M. Göken, and S. Neumeier: *Scr. Mater.*, 2021, vol. 200, p. 113928.
44. V.A. Vorontsov, T.P. McAuliffe, M.C. Hardy, D. Dye, and I. Bantounas: *Acta Mater.*, 2022, vol. 232, p. 117936.
45. M.K. Miller and K.F. Russell: *Ultramicroscopy*, 2007, vol. 107, pp. 761–66.
46. F.D. León-Cázares, F. Monni, and C.M.F. Rae: *Acta Mater.*, 2020, vol. 199, pp. 209–24.
47. A. Bezold and S. Neumeier: *SSRN J.*, <https://doi.org/10.2139/ssrn.4180430>.

48. L.P. Freund: Doctoral dissertation, University Erlangen-Nürnberg, 2018.
49. L.P. Freund, A. Stark, F. Pyczak, N. Schell, M. Göken, and S. Neumeier: *J. Alloy. Compd.*, 2018, vol. 753, pp. 333–42.
50. S.C.H. Llewelyn, K.A. Christofidou, V.J. Araullo-Peters, N.G. Jones, M.C. Hardy, E.A. Marquis, and H.J. Stone: *Acta Mater.*, 2017, vol. 131, pp. 296–304.
51. C.H. Zenk, N. Volz, C. Zenk, P.J. Felfer, and S. Neumeier: *Crystals*, 2020, vol. 10, p. 1058.
52. G.B. Viswanathan, P.M. Sarosi, M.F. Henry, D.D. Whitis, W.W. Milligan, and M.J. Mills: *Acta Mater.*, 2005, vol. 53, pp. 3041–057.
53. R.R. Unocic, G.B. Viswanathan, P.M. Sarosi, S. Karthikeyan, J. Li, and M.J. Mills: *Mater. Sci. Eng., A*, 2008, vol. 483–484, pp. 25–32.
54. D.J. Crudden, A. Mottura, N. Warnken, B. Raesinia, and R.C. Reed: *Acta Mater.*, 2014, vol. 75, pp. 356–70.
55. T. Kruml, E. Conforto, B. Lo Piccolo, D. Caillard, and J.L. Martin: *Acta Materialia*, 2002, vol. 50, pp. 5091–5101.
56. M. Dodaran, A.H. Etefagh, S.M. Guo, M.M. Khonsari, W.J. Meng, N. Shamsaei, and S. Shao: *Intermetallics*, 2020, vol. 117, p. 106670.
57. K. Vamsi and S. Karthikeyan: in *Superalloys 2012 (Twelfth International Symposium)*, John Wiley & Sons, Inc., 2012, pp. 521–30.
58. A. Breidi, J. Allen, and A. Mottura: *Acta Mater.*, 2018, vol. 145, pp. 97–108.
59. A. Mottura, A. Janotti, and T.M. Pollock: *Intermetallics*, 2012, vol. 28, pp. 138–43.
60. L. Feng, D. Lv, R.K. Rhein, J.G. Goiri, M.S. Titus, A. Van der Ven, T.M. Pollock, and Y. Wang: *Acta Mater.*, 2018, vol. 161, pp. 99–109.

Publisher's Note Springer Nature remains neutral with regard to jurisdictional claims in published maps and institutional affiliations.